Rashba spin splitting and photocatalytic properties of GeC-*M*SSe (*M* = Mo, W) van der Waals heterostructures

H. U. Din,[1] M. Idrees,[1] Arwa Albar,[2] M. Shafiq,[3] Iftikhar Ahmad,[3,*] Chuong V. Nguyen,[4,†] and Bin Amin[3,‡]

[1]*Department of Physics, Hazara University, Mansehra 21300, Pakistan*

[2]*Department of Physics, College of Science, Jeddah University, Jeddah 21589, Saudi Arabia*

[3]*Abbottabad Uniersity of Science and Technology, Abbottabad 22010, Pakistan*

[4]*Department of Materials Science and Engineering, Le Quy Don Technical University, Ha Noi 100000, Vietnam*

(Received 15 July 2019; revised manuscript received 15 October 2019; published 28 October 2019)

Vertical stacking of ultrathin two-dimensional materials via weak van der Waals (vdW) interactions is identified as an important technique for tuning the physical properties and designing viable products for nanoelectronics, spintronics, and renewable energy source applications. The geometry, electronic, and photocatalytic properties of vdW heterostructures of GeC and Janus transition metal dichalcogenides *M*SSe (*M* = Mo, W) monolayers are investigated by performing first-principles calculations. Two different possible models of GeC-*M*SSe heterostructures are presented with an alternative order of chalcogen atoms at opposite surfaces in *M*SSe. The most favorable stacking pattern of both models is dynamically and energetically feasible. A direct type-II band alignment is obtained in both models of understudy heterobilayer systems. The spin orbit coupling (SOC) effect causes considerable Rashba spin splitting in both *M*SSe monolayers. In particular, a greater Rashba spin polarization is demonstrated in model 1 (GeC-WSSe) than model 2 (GeC-MoSSe) caused by the alternative order of chalcogen atoms and larger SOC effect of heavier W than Mo atoms, which provides a platform for experimental and theoretical understanding of designing two-dimensional spintronic devices. More interestingly, the appropriate band alignments of model 1 with the standard water redox potentials enable its capability to dissociate water into H^+/H_2 and O_2/H_2O. In contrast to model 1, model 2 can only oxidize water into O_2/H_2O. The simulated design of GeC-*M*SSe is predicted for promising use in future electronic, spintronics, and photocatalytic water splitting.

DOI: 10.1103/PhysRevB.100.165425

I. INTRODUCTION

Interest in the field of two-dimensional (2D) materials, after the successful synthesis of graphene [1], has led the emergence of one-atom-thick materials exhibiting extraordinary electronic and optical properties [2–4]. Beyond the gapless single layer graphene, 2D transition-metal dichalcogenidies (TMDCs) with general formula MX_2 (M = Mo, W; X = S, Se) have been extensively studied due to their fascinating properties [5,6]. In particular, the high structure stability, suitable band-gap nature (ranging from 1.0 to 1.9 eV), and strong coupling between spin and valley degrees of freedom [7–9] make these materials potential candidates for optoelectronics, field effect transistors (FETs), solar cells, and photocatalytic applications [10–13]. Apart from these exciting properties, TMDCs lack electric-controlled spin precession and Rashba spin-orbit coupling (SOC), thus limiting their applications in spin FETs [14].

Recently, selenization in MoS_2 [15] and sulfurization in $MoSe_2$ [16] through chemical vapor deposition (CVD) have successfully confirmed Janus MoSSe monolayers. Also, single layers of WSSe have been prepared by CVD method [17,18]. The space group 2H-MX_2 is changed from D_{3h} to C_{3v} for Janus MXY (M = Mo, W; X, Y = S, Se) monolayers [19,20]. Xia *et al.* [14] recently reported the energetic feasibility and universality of electronic and photocatalytic properties of Janus MXY monolayers. SOC-induced Rashba spin splitting in these polar Janus MXY monolayers has also been demonstrated [21]. It was shown that WSeTe monolayer has a significant Rashba spin splitting in the electronic band dispersion caused by intrinsic out-of-plane electric field induced due to the mirror asymmetry. The giant Rashba spin splitting in these single layers of Janus MXY renders their potentiality for out-of-plane piezoelectricity and future spintronic device applications [22,23].

Besides TMDCs and Janus TMDCs, the graphenelike hexagonal 2D compounds of group IV elements have also been gaining considerable attention due to their direct band-gap nature, which makes them a suitable candidate for designing optoelectronics, photovoltaic devices, and heterostructures [24–26]. GeC thin films have been prepared by laser ablation [27,28] and CVD techniques [29]. It has been reported that 2D GeC has a dynamically stable planar structure and exhibits excellent electronic and optical properties [30–32]. The single-layer GeC has higher Poisson's ratio and lower stiffness compared to graphene [33]. Thus, the outstanding performance of single-layer GeC enables it for achieving

*ahma5532@gmail.com

†Corresponding author: chuongnguyen11@gmail.com

‡Corresponding author: binukhn@gmail.com

enhanced electronic, optoelectronic, and photovoltaic device applications [34].

Heterostructures formed by combining distinct 2D materials have been extensively identified as a useful tool to tune the electronic behavior, resulting in exciting physical phenomena which play a key role in nanoscale electronic and photovoltaic devices [35–39]. As a consequence, the vertically stacked 2D TMDCs via weak van der Waals (vdW) interaction are termed vdW heterostructures and exhibit type-II band alignment [40,41]. In type-II band alignment, the electrons in the conduction band (CB) and holes in the valence band (VB) are localized in different constituents, resulting in the charge carrier separation which is crucial for photodetection and energy-harvesting purposes [42]. Moreover, the photocatalytic water splitting under solar irradiation for photogenerating electrons and holes is also explored in TMDC-TMDC heterostructures [43]. Generally, in the composite semiconductor system with type-II heterojunctions, the VB and CB of semiconductor A are higher than that of semiconductor B, thus the photogenerated electrons will migrate from the CB of semiconductor A to that of semiconductor B with a lower reduction potential, and the corresponding holes in the VB of semiconductor B will migrate to semiconductor A with a lower oxidation potential, thus a spatial separation of electron-hole pairs will be completed. Consequently, the type II heterojunction is the most effective structure for improving the photocatalysis performance of semiconductors [44–46]. Recently, type-II band alignment and enhanced photocatalytic response for water splitting have been reported in SiC-TMDCs [47] and GeC-TMDCs [48] vdW heterostructures. In addition, Li *et al.* [49] have addressed a large Rashba spin polarization, type-II band alignment and tunable electronic character in Janus MoSSe-WSSe vdW heterostructures. Despite these preliminary achievements, the fundamental electronic and photocatalytic properties of GeC and Janus *M*SSe vdW heterostructures remain unexplored.

In this paper, inspired by the highly energetic feasibility and satisfying lattice mismatch, we propose the vdW heterostructures of GeC and Janus *M*SSe to demonstrate the unprecedented properties by first-principles calculations. Two different models of vdW heterostructures based on the alternative order of chalcogen atoms with six possible stacking configurations are presented. It is found that both models with most favorable stacking configurations are dynamically stable. Further, a comprehensive insight is gained to explore the electronic properties, including Rashba spin spilitting and photocatalytic response of the most stable configuration. More interestingly, both models exhibit type-II semiconducting band-gap nature and considerable Rashba spin splitting parameters. The findings raised potential applications of constructing vdW heterostructures for designing nanoelectronic and photovoltaic devices.

II. COMPUTATIONAL DETAILS

We performed density-functional theory calculations with projector-augmented plane wave scheme in VIENNA AB INITIO SIMULATION PACKAGE [50–52]. The Grimme [53] vdW correction with 500 eV cutoff was used in Perdew-Burke-Ernzerhof (PBE) [54] functional to optimize the geometry until the forces and energy converged to 10^{-4} eV/Å and 10^{-5} eV, respectively. A $6 \times 6 \times 1\Gamma$-centered Monkhorst-Pack k-mesh is used for structural relaxation, which is further refined to $12 \times 12 \times 1$ for optimized structure. Artifacts of the periodic boundary conditions prevented by a vacuum layer of 25 Å were added along the z axis.

It is common that PBE functional underestimates the band-gap values of semiconductors, therefore, HSE06 (Heyd-Scuseria-Ernzerhof) functional [55] is also used for electronic-structure calculations. However, due to high computational cost, HSE06 calculations are avoided to refine the k-mesh. SOC effect is significant in TMDCs and Janus monolayers, hence, SOC is also taken into account in our calculations. The SOC is incorporated by a second variational method [56], which uses scalar-relativistic basis, based on the reduction of original basis. In the variational method, the scalar relativistic part of the Hamiltonian is diagonlized in scalar relativistic basis and the calculated eigenfunctions are then used to construct the full Hamiltonian matrix including SOC and may be written as

$$\mathcal{H}\widetilde{\Psi} = \varepsilon\widetilde{\Psi} + \mathcal{H}_{\mathrm{SO}}\widetilde{\Psi}, \tag{1}$$

where $\mathcal{H}_{\mathrm{SO}}$ represents the spin-orbit Hamiltonian and is given as

$$\mathcal{H}_{\mathrm{SO}} = \frac{\hbar}{2Mc^2}\frac{1}{r}\frac{dV}{dr}\begin{pmatrix}\vec{\sigma}\vec{l} & 0\\ 0 & 0\end{pmatrix}, \tag{2}$$

where $\vec{\sigma}$ denotes the Pauli spin matrices.

Phonon spectrum calculations are performed by Phonopy code, which uses the harmonic interatomic force constants as input, obtained by density-functional perturbation theory. A $4 \times 4 \times 1$ supercell with $6 \times 6 \times 1$ k-mesh and 500 eV cutoff are used to ensure the convergence [57,58].

III. RESULTS AND DISCUSSION

Optimized lattice constant (3.26 Å, 3.25 Å, 3.26 Å) and bond-length values (1.882 Å for Ge–C, 2.419 (2.424) Å for Mo(W)–S, 2.533 (2.538) Å for Mo(W)–Se) of GeC, MoSSe, and WSSe monolayers, respectively, are agreeing well with previous reports [23,31,32,49,59], thus indicating the reliability of our computational approach. GeC and *M*SSe monolayers exhibit the same hexagonal lattices with satisfying lattice mismatches, realizing possible experimental fabrication of GeC-*M*SSe vdW heterostructures for practical applications.

In general, the interfacial properties are significantly sensitive to the specific contacted atoms and local configurations. Since S(Se)-*M*SSe terminated surfaces are available for constructing vdW heterostructures of GeC and *M*SSe monolayers, hence we consider two different models with alternate positions of S/Se atoms at opposite surfaces in *M*SSe, see Figs. 1(i)–1(ii). In model 1, stacking a(b), Ge atom is placed fixed below M atom and C atom is located below Se atom (hollow site). Stacking c(d), Ge atom is placed below Se atom and C atom is positioned at the hollow site (below *M* atom). Stacking e(f), Ge atom is fixed at the hollow site and C atom is placed below *M*(Se) atom, respectively, see Fig. 1(iii). A similar stacking pattern with an alternative position of S and

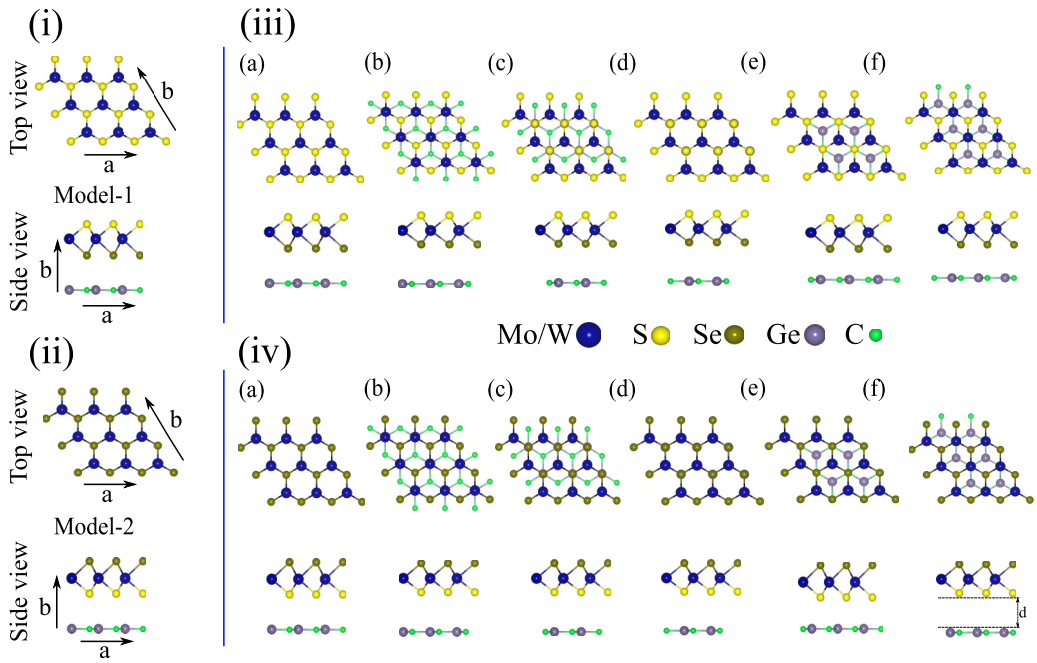

FIG. 1. Top and side view of (i) model 1 with Se atom located on bottom surface of Mo(W)SSe layer, (ii) model 2 with S atom placed at the bottom surface of Mo(W)SSe layer, and (iii), (iv) six possible stacking patterns of GeC-*M*SSe for both models (see text for details), and d represents the interlayer distance.

Se atoms in *M*SSe monolayers is also followed for model 2, see Fig. 1(iv).

The binding energy is defined as $E_b = E_{GeC\text{-}MSSe} - E_{GeC} - E_{MSSe}$, where $E_{GeC\text{-}MSSe}$, E_{GeC}, and E_{MSSe} represent the total energy of GeC-*M*SSe heterostructure, isolated GeC, and *M*SSe monolayers, respectively. The calculated binding energy (E_b), interlayer distance (d), bond length, and the optimized lattice parameters, listed in Table I, are comparable with GeC-TMDCs heterostructures [48,60]. Meanwhile, the disparity between different stacking patterns is found in the magnitude of their corresponding binding energy and interlayer distance. The most favorable stacking pattern [configuration e(b) for model 1 (model 2)] has the smallest interlayer distance, indicating higher energetic stability and strong physical interaction between GeC and *M*SSe. It is noteworthy that the larger covalent radius of Se than S atoms leads to larger vdW attractive energy which may be responsible for small differences in the interlayer distance between the favorable

TABLE I. Binding energy (E_a, E_b, E_c, E_d, E_e, and E_f), interlayer distance ($d_{spacing}$), lattice constant (a), bond length (Ge–C and M–S/Se), and band gap (E_g (PBE/PBE–SOC), E_g (HSE06/HSE06–SOC) for both models of GeC-*M*SSe heterostructures.

	GeC-MoSSe		GeC-WSSe	
Hetrostructures	Model 1	Model 2	Model 1	Model 2
E_a (eV)	−2.21	−1.91	−2.13	−1.81
$d_{spacing}$ (Å)	3.58	3.50	3.61	3.54
E_b (eV)	−3.23	−2.95	−3.11	−2.79
$d_{spacing}$ (Å)	3.24	3.11	3.27	3.14
E_c (eV)	−2.60	−2.48	−2.49	−2.30
$d_{spacing}$ (Å)	3.46	3.27	3.51	3.37
E_d (eV)	−2.86	−2.61	−2.74	−2.45
$d_{spacing}$ (Å)	3.35	3.20	3.42	3.31
E_e (eV)	−3.36	−2.88	−3.29	−2.75
$d_{spacing}$ (Å)	3.21	3.13	3.22	3.16
E_f (eV)	−2.09	−1.81	−2.03	−1.71
$d_{spacing}$ (Å)	3.63	3.55	3.26	3.26
a (Å)	3.26	3.26		
Ge–C (Å)	1.876	1.882	1.879	1.882
M–S/M–Se (Å)	2.42/2.53	2.42/2.54	2.42/2.54	2.42/2.54
E_g (PBE/PBE-SOC) (eV)	1.31/1.21	0.81/0.79	1.56/1.41	1.03/1.00
E_g (HSE/HSE-SOC) (eV)	1.87/1.86	1.31/1.30	2.16/2.06	1.62/1.58

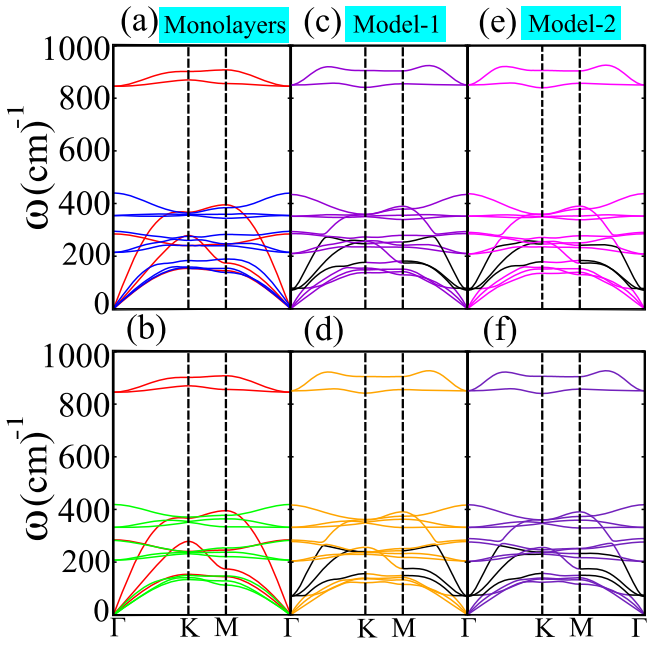

FIG. 2. Phonon spectrum of (a) GeC(MoSSe) in red (blue) (b) GeC(WSSe) in red (green) (c), (d) GeC-Mo(W)SSe in violet (orange) for model 1 (e), (f) GeC-Mo(W)SSe in magenta (indigo) for model 2, respectively.

configuration and the energetic feasibility of models 1 and 2 [60]. Also, the calculated vertical distance (d) reveals that these heterostructures possess a vdW type of interaction. The small lattice mismatch induces strain and may be responsible for the rearrangement of atoms in GeC-*M*SSe heterobilayers. Thus, the bond length of Ge-C is compressed while *M*-S (*M*-Se) is slightly stretched for both systems with different models, which is also comparable to those reported in GeC-TMDCs [48,61].

In addition, the dynamical stability of the freestanding monolayers and the corresponding most favorable configuration of both models of GeC-*M*SSe heterostructures is also verified by calculating the phonon band structure, as illustrated in Fig. 2. More interestingly, both heterostructures with favorable stacking order [configuration-e(b) for model 1 (model 2)] and their corresponding parent monolayers are free from imaginary frequency, thus confirming their dynamical stability. For GeC(*M*SSe) monolayers, 3(3) acoustic and 3(6) optical phonon branches are noted due to 2(3) atoms per unit cell, as shown in Figs. 2(a)–2(b). The calculated phonon spectrum is in good agreement with available theoretical and experimental literature [16,24,62]. In acoustic modes, the transverse acoustic and longitudinal acoustic branches lying near the Γ point are linear while slight deviation is observed in the out-of-plane acoustic mode (ZA). The corresponding ZA modes in *M*SSe and GeC-*M*SSe systems are not purely quadratic and contain components of in-plane vibrations or coupling of in-plane and out-of-plane modes due to the loss or breaking of reflection symmetry over the *xy* plane. A similar trend is also observed for other 2D materials [63–65]. However, there are five atoms per unit cell in GeC-*M*SSe heterostructures thus, 3(12) acoustic (optical) modes are found in the calculated phonon band spectra, as shown in Figs. 2(c)–2(f). In these heterostructures, the phonon band spectrum comprising lowest optical phonon branches (in the range 70–78 cm^{-1}) located near acoustic branches at the Γ point is indicating the weak interlayer coupling and weak vdW interactions. A similar trend is also experimentally observed in TMDC-TMDC heterostructures [66] and theoretically demonstrated in SiC-TMDCs [47], P-SiC [67], and MXenes-TMDCs [68] heterostructures.

Behavior of the band structure and band-gap values of *M*SSe monolayers are sensitive to the exchange-correlation functional and SOC effect. Therefore, for comparison, the electronic band structures of the isolated monolayers and their corresponding heterostructures are calculated at PBE and HSE06 level with and without including the SOC effect. The isolated GeC and *M*SSe monolayers exhibit direct semiconducting band-gap nature with valence band maximum (VBM) and conduction band minimum (CBM) located at *K*-point of Brillouin zone (BZ). Magnitude of band gap using PBE/HSE06 functional is 2.09/3.01 eV for GeC, 1.46/2.06 eV (with SOC) for MoSSe and 1.37/2.07 eV (with SOC) for WSSe, which are well consistent with available literature [24,31,32,49,59]. As *M*SSe monolayers are strongly affected by SOC effect, therefore SOC band-gap values are presented for better comparison to most of the available literature. Moreover, SOC causes no prominent band splitting in GeC. The direct band-gap nature of these monolayers makes them feasible in optoelectronic [30] and photovoltaic devices [14].

It is obvious from Fig. 3 that both GeC-*M*SSe heterobilayers with different stacking models reveal the direct band-gap nature with VBM and CBM located at the *K*-point of BZ. The calculated band-gap values (without and with SOC), the Rashba spin splitting, and the band spin splitting Γ_v and λ_v along the uppermost VB and lowermost CB, respectively, in understudy monolayers, as listed in Tables I and II, are consistent with previous works [21,49,60]. According to Table I, the band-gap values at HSE06 theory level are larger than those obtained at PBE and further reduced by CB and/or VB spin splitting caused by SOC and mirror asymmetry in *M*SSe. However, the magnitude of the band gap increases (decreases) from Mo (model 1) to W (model 2) in the GeC-*M*SSe system. Since a local maximum in the VB and/or a local minimum in the CB is known as a valley and the band structure of an ideal valleytronic material is composed of two or more degenerate inequivalent valley states [69]. The CB and VB edges of the understudy heterobilayer systems are characterized by the energetically degenerate valleys, which is crucial for valleytronics. These special energy valleys are marked as λ_{kc}, λ_{kv}, and λ_v, schematically represented in Fig. 3(e) (1 and 2).

It is clear from Table II that in contrast to MoSSe and WSSe monolayers, both λ_{kc} and λ_{kv} increases from Mo to W (due to greater atomic number of heavier W than Mo) and significantly larger λ_{kc} is also found than λ_{kv} (except GeC-WSSe at PBE-SOC level), making them prominent for valleytronics [21,49]. Like MoSSe and WSSe monolayers, the λ_{kc} and λ_v valleys are composed of out-of-plane orbital (Mo/W-dz^2) while λ_{kv} is occupied by p_z orbital of C atom. For GeC-*M*SSe heterobilayers, the lowermost CB is more promising for valleytronic applications as compared to the topmost VB

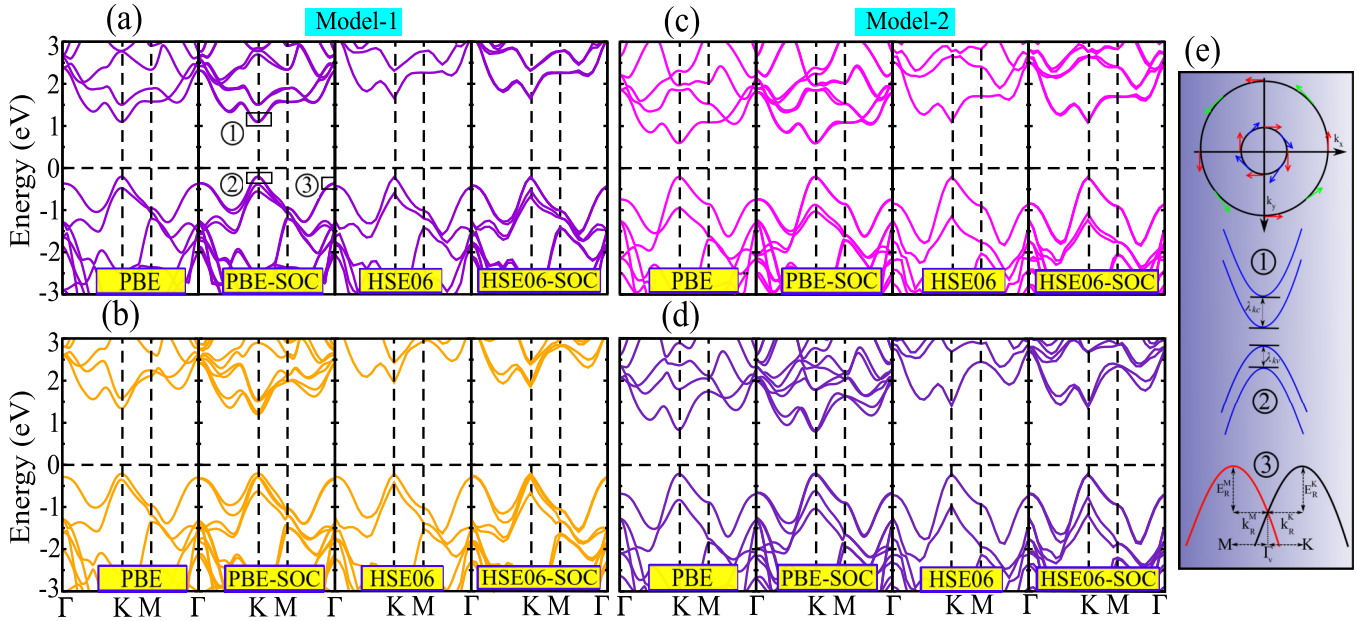

FIG. 3. Band structure of (a), (b) GeC-Mo(W)SSe in violet (orange) for model 1 (c), (d) GeC-Mo(W)SSe in magenta (indigo) for model 2. (e) Schematic of spin texture of two bands around Γ_v, and the encircled numbers (1, 2, and 3) represent the magnified view of valence band-, conduction band-splitting at *K*-point and Rashba spin splitting around Γ_v, respectively.

due to enhanced spin splitting (λ_{kc}) at *K*-point [8,21,49]. It is noticeable that the choice of exchange-correlation functional strongly affects the size of SO splitting [7]. This is likely because PBE is the local exchange-correlation functional while HSE addresses the influence of the nonlocal exchange correlation functional [70,71]. Obviously, a large spin splitting λ_{kc}, λ_{kv}, and λ_v is observed at HSE06-SOC level than PBE-SOC, thus accounting for no Rashba effect along Γ_v of BZ. Interestingly, the Rashba spin splitting with different magnitudes for all understudy heterobilayer systems is obtained around Γ point in VB by PBE-SOC, see the zoom-in schematic illustration in Fig. 3(e) (3). As HSE06-SOC results in no Rashba spin splitting at Γ point and the lack of previous theoretical and experimental work for comparison encourage us to mainly focus on PBE-SOC level for further understanding of Rashba spin splitting.

The spin polarization of two topmost bands at Γ_v-point in VB are opposite and satisfy $\sigma(-k) = -\sigma(k)$. Additionally, we plot the spin texture, where the spin arrows in the zone center rotating in a clockwise pattern are responsible for Rashba spin splitting, see Fig. 3(e). Generally, the Rashba spin splitting is defined as $\alpha_R^{K/M} = 2E_R^{K/M}/k_R^{K/M}$, where $\alpha_R^{K/M}$, $E_R^{K/M}$, and $k_R^{K/M}$ represent Rashba parameter, Rashba energy, and momentum offset along $\Gamma - K/\Gamma - M$ directions, respectively [72]. The slightly different values of α_R^M from α_R^K as presented in Table II, indicating that Rashba parameters are not sensitive to the directions selected in the BZ for these mono- and heterobilayers. Moreover, the calculated Rashba parameter increases from model 1 (GeC-MoSSe)/MoSSe to model 2 (GeC-WSSe)/WSSe are due to the larger SOC effect of heavier W than Mo and selective order of chalcogen atoms in GeC-*M*SSe heterobilayers [72]. Hence, these vdW

TABLE II. The valence band splitting λ_{kc} (MeV) at the VBM, conduction band splitting λ_{kv} (MeV) at the CBM, Rashba energy (E_R^K and E_R^M in MeV), momentum offset (k_R^K and k_R^M in Å^{-1}, and Rashba parameter (α_R^K and α_R^M in eV) along $\Gamma - K$ and $\Gamma - M$ directions, respectively, at PBE and HSE06 levels with SOC for corresponding MoSSe, WSSe monolayers, and their corresponding heterostructures.

			λ_{kc}	λ_{kv}	Γ_v	E_R^K	k_R^K	α_R^K	E_R^M	k_R^M	α_R^M
Monolayers	MoSSe	PBE–SOC	13.7	170	–	1.40	0.005	0.54	1.40	0.007	0.42
		HSE–SOC	20.6	165	6.20	–	–	–	–	–	–
	WSSe	PBE–SOC	26.8	449	–	2.90	0.008	0.75	2.90	0.007	0.86
		HSE–SOC	25.8	446	20.9	–	–	–	–	–	–
Model 1	GeC-MoSSe	PBE–SOC	11.5	1.80	–	0.60	0.003	0.46	0.60	0.005	0.27
		HSE–SOC	25.7	2.50	6.20	–	–	–	–	–	–
	GeC-WSSe	PBE–SOC	53.3	81.4	–	2.10	0.005	0.81	2.10	0.007	0.62
		HSE–SOC	63.8	50.7	19.7	–	–	–	–	–	–
Model 2	GeC-MoSSe	PBE–SOC	14.2	1.10	–	0.80	0.005	0.31	0.70	0.007	0.21
		HSE–SOC	21.4	2.70	7.02	–	–	–	–	–	–
	GeC-WSSe	PBE–SOC	22.0	18.3	–	1.90	0.005	0.73	1.90	0.007	0.57
		HSE–SOC	26.8	18.1	20.5	–	–	–	–	–	–

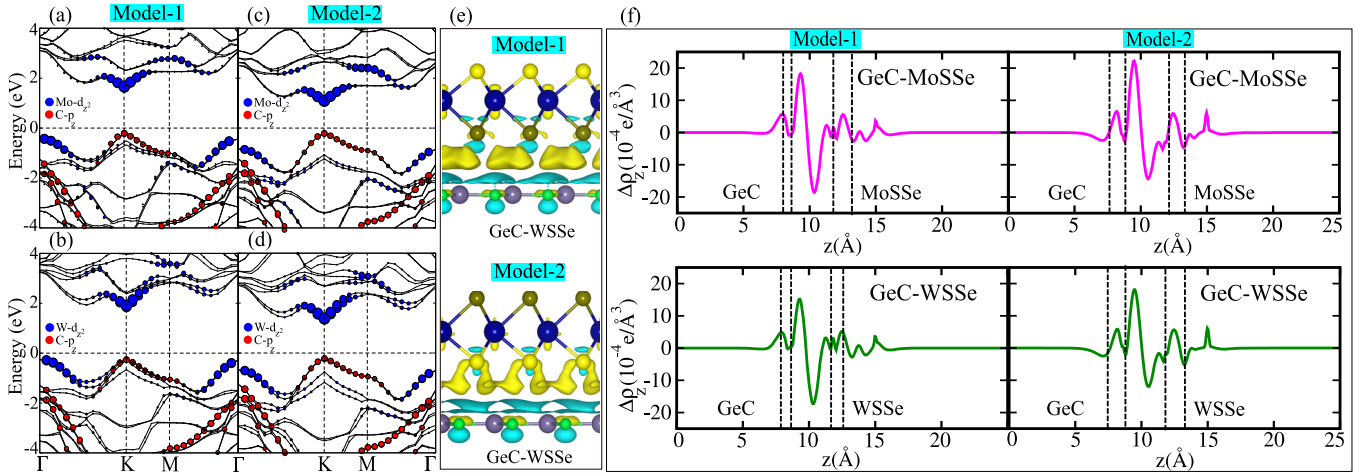

FIG. 4. Weighted band structure of (a), (b) GeC-Mo(W)SSe for model 1 (c), (d) GeC-Mo(W)SSe for model 2. (e) Schematic of charge density difference (with isovalue 0.00023 e/Bohr^3), where the yellow and cyan colors represent the charge depletion and charge accumulation, and (f) planar-averaged charge density of GeC-Mo(W)SSe for model 1 and model 2, respectively.

heterostructures with considerable Rashba spin splitting sets a platform for practical applications in future spintronics.

Further, deep insight is gained into the band alignment of GeC-*M*SSe heterostructures by introducing the projected weighted bands using HSE06-SOC, depicted in Figs. 4(a)–4(d). One can clearly note that VBM is mainly contributed by the C-p_z orbital while the out-of-plane orbital (Mo/W-d_{z^2}) makes the largest contribution to the lowermost of the CB. Obviously, VBM and CBM in GeC-*M*SSe are localized in GeC and *M*SSe monolayers, indicating type-II band alignment (staggered type). A type-II band alignment is crucial for charge carrier separation and is also reported in SiC-TMDCs, MoSSe-WSSe, GeC-TMDCs, SiC-ZnO, and TMDCs-TMDCs, [47,49,61,73,74]. It is expected that the photogenerated charge carriers (electrons) move from GeC to *M*SSe layer and the holes are transferred from *M*SSe to GeC, which could effectively decrease the rate of charge recombination. Consequently, GeC-*M*SSe heterobilayers deserve promising considerations in solar cells [73,74].

To address the specific interlayer charge transfer, the charge density difference is shown in Fig. 4(e). The charge density difference ($\Delta\rho$), defined as $\Delta\rho = \rho_{\text{hetero}} - \rho_{\text{GeC}} - \rho_{M\text{SSe}}$, where ρ_{hetero}, ρ_{GeC}, and $\rho_{M\text{SSe}}$ represent the charge density of heterostructure, GeC, and *M*SSe monolayers, respectively. It is demonstrated that the electrons are transferred from GeC to *M*SSe, however, the charge redistribution is mainly found in the interfacial region between the C atom and adjacent Se/S atom due to difference in their electronegativity. As both models of GeC-MoSSe and GeC-WSSe share the same character of charge density difference pattern, $\Delta\rho$ is presented only for different models of GeC-WSSe heterostructures, see Fig. 4(e). To offer more details of charge redistribution, the planar-averaged charge density is estimated versus z direction normal to heterostructures, see Fig. 4(f). The positive value of planar-averaged charge density indicates that GeC donates electrons to *M*SSe monolayers, realizing p-type doping in GeC and n-type doping in *M*SSe. In addition, Bader charge analysis [75] is performed to get a better understanding of this charge transfer process from GeC to *M*SSe. It is found that from GeC, a 0.024 e (0.035 e) amount of charge is transferred to MoSSe in the model 1 (model 2) heterostructure. Similarly, a 0.020 e(0.029 e) is transferred to WSSe in the model 1 (model 2) heterostructure. These values indicate that for all understudy heterobilayer systems, the GeC layer donates electrons and *M*SSe accepts electrons (electron loss and gain is represented by yellow and cyan colors, respectively, in Fig. 4(e), thus leading to p-doping in GeC and n-doping in *M*SSe. Moreover, the charge transfer between C and Se/S atoms induces a built in electric field which spatially separates the photogenerated charge carriers in different constituents. This indicates the weak interaction between GeC and *M*SSe, which has also been demonstrated SiC-TMDCs and GeC-TMDCs [47,67]. Interestingly, it reveals for MoSSe in model 1 a charge transfer from Mo to S and for WSSe in model 1 a charge transfer from W to S, suggesting that model 1 yields stronger electronic influence.

For further exploration into hydrogen production by water splitting under the irradiation of solar energy, the band-edge positions of CB and VB with the oxidation and reduction potentials of splitting water are computed using the HSE06-SOC level. In general, the standard reduction (H^+/H_2) and oxidation (O_2/H_2O) potentials can be written as $E^{\text{red}}_{H^+/H_2} = -4.44\ \text{eV} + \text{pH} \times 0.059\ \text{eV}$ and $E^{OX}_{O_2/H_2O} = -5.67\ \text{eV} + \text{pH} \times 0.059\ \text{eV}$ [48]. The photocatalytic process involves the separation and transportation of photogenerated electrons to H^+/H_2 or holes to O_2 molecules. For water splitting, the band gap of photocatalysts should be larger than 1.23 eV. Also, it has been reported that the overpotential required to split water is linked to restrictions on the electron's spin [76]. In addition, many theoretical or experimental findings reveal that spin flipping in the honeycomb lattice plays a key role in the charge transport and separation and can enhance spin-orbit interactions [77–79]. The Rashba spin splitting of bands close to the band gap, arising from SOC in locally polarized domains, makes the tunneling channels flip

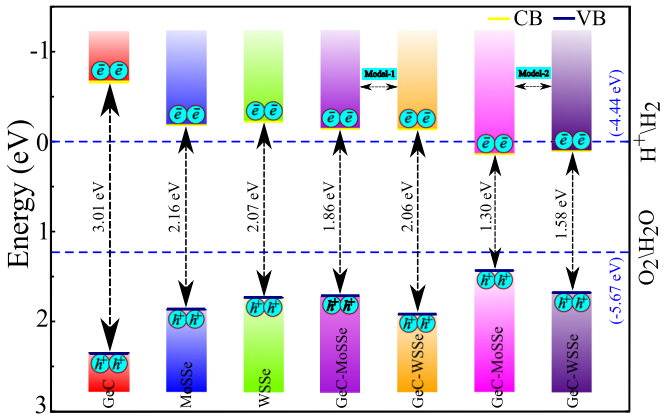

FIG. 5. The valence band (VB) and conduction band (CB) edge alignment of GeC, MoSSe, WSSe and their corresponding heterostructures; the blue dashed-lines represent the standard oxidation (−5.67 eV) and reduction (−4.44 eV) potentials for water splitting into O_2/H_2O and H^+/H_2, respectively.

and govern the charge carrier recombination, which eventually controls the carrier lifetime, diffusion length, and results in the superior electron transmission performance for photocatalysis [80–82]. This highlights that a highly active H_2 and O_2 evolution can be achieved over a photocatalyst under visible light irradiation, thus leading to significant photocatalytic activity [80].

The band edge position of the freestanding monolayer and their corresponding heterostructures with respect to the standard reduction (−4.44 eV) and oxidation (−5.67 eV) potentials for water splitting at pH = 0 is displayed in Fig. 5. It can be clearly seen that both CB and VB edges of GeC, MoSSe, and WSSe monolayers are located more negative and more positive than the redox potential of H^+/H_2 and O_2/H_2O, respectively, which is in good agreement with previous works [83,84]. This suggests that the water reduction and oxidation reactions may be thermodynamically feasible for the possible vdW heterostructures. More interestingly, the energy level of CB and VB for GeC-Mo(W)SSe (model 1) heterobilayers is higher than the standard redox potentials, providing enough force to drive the phototgenerated electrons and holes to dissociate water into H^+/H_2 and O_2/H_2O, thus making it promising for photocatalytic water splitting. In GeC-*M*SSe (model 2), the CB edge straddles the oxidation potential while the VB edge is significantly lower than the reduction potential and thus fails to reduce water into H^+/H_2. In contrast to model 1, this illustrates the suppressed photocatalytic response of the model 2 heterobilayer system. Hence, it indicates that the photocatalytic water splitting is highly sensitive to the relative order of chalcogen atoms in *M*SSe monolayers by vdW stacking with GeC monolayer. A similar trend is also demonstrated for SiC-TMDCs and TMDC-TMDCs [43,47]. We propose GeC-*M*SSe (model 1) heterostructures as exciting materials for photocatalytic water splitting and suggest them promising for low-cost and large-scale production of solar hydrogen.

IV. CONCLUSION

In summary, we have systematically investigated the geometric, electronic, and photocatalytic properties of the vdW heterostructures of GeC and Janus TMDCs *M*SSe (*M* = Mo, W) by first-principles calculations. Our findings indicate that the most favorable vdW stacking of GeC with *M*SSe via alternative order of chalcogen atoms at opposite surfaces in *M*SSe is energetically and dynamically feasible. Both models reveal direct type-II band semiconducting nature, which facilitates the charge carrier separation and is highly desirable for solar cell. The Rashba spin splitting caused by SOC effect is observed in *M*SSe monolayers. More interestingly, larger Rashba spin splitting is found in model 1 (GeC-WSSe) than model 2 (GeC-MoSSe) due to alternative order of chalcogen atoms and larger SOC effect of heavier W than Mo atoms, invoking attention for theoretical and experimental realization of 2D spintronic devices. In addition, the CB and VB edges of model 1(GeC-*M*SSe) straddle the standard redox potentials for water splitting and are useful for dissociating water into H^+/H_2 and O_2/H_2O. In contrast to model 1, both heterobilayers in model 2 possess suppressed photocatalytic response and fails to reduce water into H^+/H_2. The different models presented in this paper pave the way for designing electronic, spintronic, and future renewable energy devices.

ACKNOWLEDGMENTS

This research is funded by Vietnam National Foundation for Science and Technology Development (NAFOSTED) under Grant Number 103.01-2019.05. B.A. acknowledges support from the Higher Education Commission of Pakistan (HEC) under Project No. 5727/KPK/NRPU/R&D/HEC2016.

[1] K. S. Novoselov, A. K. Geim, S. V. Morozov, D. Jiang, Y. Zhang, S. V. Dubonos, I. V. Grigorieva, and A. A. Firsov, Science **306**, 666 (2004).

[2] R. R. Nair, P. Blake, A. N. Grigorenko, K. S. Novoselov, T. J. Booth, T. Stauber, N. M. Peres, and A. K. Geim, Science **320**, 1308 (2008).

[3] Y. Zhang, Y.-W. Tan, H. L. Stormer, and P. Kim, Nature **438**, 201 (2005).

[4] Z. Kahraman, A. Kandemir, M. Yagmurcukardes, and H. Sahin, J. Phys. Chem. C **123**, 4549 (2019).

[5] Q. H. Wang, K. Kalantar-Zadeh, A. Kis, J. N. Coleman, and M. S. Strano, Nat. Nanotechnol. **7**, 699 (2012).

[6] J. Kang, S. Tongay, J. Zhou, J. Li, and J. Wu, Appl. Phys. Lett. **102**, 012111 (2013).

[7] A. Kuc and T. Heine, Chem. Soc. Rev. **44**, 2603 (2015).

[8] D. Xiao, G.-B. Liu, W. Feng, X. Xu, and W. Yao, Phys. Rev. Lett. **108**, 196802 (2012).

[9] K. F. Mak, K. He, J. Shan, and T. F. Heinz, Nat. Nanotechnol. **7**, 494 (2012).

[10] Z. Yin, H. Li, H. Li, L. Jiang, Y. Shi, Y. Sun, G. Lu, Q. Zhang, X. Chen, and H. Zhang, ACS Nano **6**, 74 (2011).

[11] Y. Xie, B. Zhang, S. Wang, D. Wang, A. Wang, Z. Wang, H. Yu, H. Zhang, Y. Chen, M. Zhao *et al.*, Adv. Mater. **29**, 1605972 (2017).

[12] A. Pospischil, M. M. Furchi, and T. Mueller, Nat. Nanotechnol. **9**, 257 (2014).

[13] B. Chen, Y. Meng, J. Sha, C. Zhong, W. Hu, and N. Zhao, Nanoscale **10**, 34 (2018).

[14] C. Xia, W. Xiong, J. Du, T. Wang, Y. Peng, and J. Li, Phys. Rev. B **98**, 165424 (2018).

[15] A.-Y. Lu, H. Zhu, J. Xiao, C.-P. Chuu, Y. Han, M.-H. Chiu, C.-C. Cheng, C.-W. Yang, K.-H. Wei, Y. Yang *et al.*, Nat. Nanotechnol. **12**, 744 (2017).

[16] J. Zhang, S. Jia, I. Kholmanov, L. Dong, D. Er, W. Chen, H. Guo, Z. Jin, V. B. Shenoy, L. Shi, and J. Lou, ACS Nano **11**, 8192 (2017).

[17] X. Duan, C. Wang, Z. Fan, G. Hao, L. Kou, U. Halim, H. Li, X. Wu, Y. Wang, J. Jiang, A. P. Pan, Y. Huang, R. Yu, and X. Duan, Nano Lett. **16**, 264 (2015).

[18] S. D. Karande, N. Kaushik, D. S. Narang, D. Late, and S. Lodha, Appl. Phys. Lett. **109**, 142101 (2016).

[19] M. A. U. Absor, I. Santoso, Harsojo, K. Abraha, H. Kotaka, F. Ishii, and M. Saito, J. Appl. Phys. **122**, 153905 (2017).

[20] R. K. Defo, S. Fang, S. N. Shirodkar, G. A. Tritsaris, A. Dimoulas, and E. Kaxiras, Phys. Rev. B **94**, 155310 (2016).

[21] Y. Cheng, Z. Zhu, M. Tahir, and U. Schwingenschlögl, Europhys. Lett. **102**, 57001 (2013).

[22] L. Dong, J. Lou, and V. B. Shenoy, ACS Nano **11**, 8242 (2017).

[23] Q.-F. Yao, J. Cai, W.-Y. Tong, S.-J. Gong, J.-Q. Wang, X. Wan, C.-G. Duan, and J. H. Chu, Phys. Rev. B **95**, 165401 (2017).

[24] A. Hao, X. Yang, X. Wang, Y. Zhu, X. Liu, and R. Liu, J. Appl. Phys. **108**, 063531 (2010).

[25] S. Lin, Y. Lu, J. Xu, S. Feng, and J. Li, Nano Energy **40**, 122 (2017).

[26] J. Szmidt, M. Gazicki-Lipman, H. Szymanowski, R. Mazurczyk, A. Werbowy, and A. Kudła, Thin Solid Films **441**, 192 (2003).

[27] H. Yuan and R. S. Williams, Chem. Mater. **5**, 479 (1993).

[28] H. Shafi, A. Mahmood, Z. Ali, and M. Mehmood, in *Key Engineering Materials*, Vol. 442 (Trans Tech Publications, 2010), pp. 178–186.

[29] X. Wu, W. Zhang, L. Yan, and R. Luo, Thin Solid Films **516**, 3189 (2008).

[30] L. Drissi and F. Ramadan, Physica E **74**, 377 (2015).

[31] H. Şahin, S. Cahangirov, M. Topsakal, E. Bekaroglu, E. Akturk, R. T. Senger, and S. Ciraci, Phys. Rev. B **80**, 155453 (2009).

[32] L. Pan, H. Liu, Y. Wen, X. Tan, H. Lv, J. Shi, and X. Tang, Phys. Lett. A **375**, 614 (2011).

[33] Q. Peng, C. Liang, W. Ji, and S. De, Mech. Mater. **64**, 135 (2013).

[34] K. Ren, M. Sun, Y. Luo, S. Wang, Y. Xu, J. Yu, and W. Tang, Phys. Lett. A **383**, 1487 (2019).

[35] A. K. Geim and I. V. Grigorieva, Nature **499**, 419 (2013).

[36] B. Amin, T. P. Kaloni, and U. Schwingenschlögl, Res. Adv. **4**, 34561 (2014).

[37] Q. Sun, Y. Dai, Y. Ma, W. Wei, and B. Huang, J. Phys. Chem. Lett. **6**, 2694 (2015).

[38] W. Xia, L. Dai, P. Yu, X. Tong, W. Song, G. Zhang, and Z. Wang, Nanoscale **9**, 4324 (2017).

[39] K. D. Pham, N. N. Hieu, H. V. Phuc, I. Fedorov, C. Duque, B. Amin, and C. V. Nguyen, Appl. Phys. Lett. **113**, 171605 (2018).

[40] M.-H. Chiu, C. Zhang, H.-W. Shiu, C.-P. Chuu, C.-H. Chen, C.-Y. S. Chang, C.-H. Chen, M.-Y. Chou, C.-K. Shih, and L.-J. Li, Nat. Commun. **6**, 7666 (2015).

[41] L. Kou, T. Frauenheim, and C. Chen, J. Phys. Chem. Lett. **4**, 1730 (2013).

[42] R. Bose, G. Manna, S. Jana, and N. Pradhan, Chem. Commun. **50**, 3074 (2014).

[43] B. Amin, N. Singh, and U. Schwingenschlögl, Phys. Rev. B **92**, 075439 (2015).

[44] J. Ge, Y. Zhang, Y.-J. Heo, and S.-J. Park, Catalysts **9**, 122 (2019).

[45] A. Shirmardi, M. A. M. Teridi, H. R. Azimi, W. J. Basirun, F. Jamali-Sheini, and R. Yousefi, Appl. Surf. Sci. **462**, 730 (2018).

[46] M. T. Uddin, Y. Nicolas, C. Olivier, T. Toupance, L. Servant, M. M. Müller, H.-J. Kleebe, J. Ziegler, and W. Jaegermann, Inorg. Chem. **51**, 7764 (2012).

[47] H. Din, M. Idrees, G. Rehman, C. V. Nguyen, L.-Y. Gan, I. Ahmad, M. Maqbool, and B. Amin, Phys. Chem. Chem. Phys. **20**, 24168 (2018).

[48] K. Ren, C. Ren, Y. Luo, Y. Xu, J. Yu, W. Tang, and M. Sun, Phys. Chem. Chem. Phys. **21**, 9949 (2019).

[49] F. Li, W. Wei, P. Zhao, B. Huang, and Y. Dai, J. Phys. Chem. Lett. **8**, 5959 (2017).

[50] W. Kohn and L. J. Sham, Phys. Rev. **140**, A1133 (1965).

[51] G. Kresse and J. Hafner, Phys. Rev. B **47**, 558 (1993).

[52] P. E. Blöchl, Phys. Rev. B **50**, 17953 (1994).

[53] S. Grimme, J. Comput. Chem. **27**, 1787 (2006).

[54] J. P. Perdew, K. Burke, and M. Ernzerhof, Phys. Rev. Lett. **77**, 3865 (1996).

[55] J. Heyd, G. E. Scuseria, and M. Ernzerhof, J. Chem. Phys. **118**, 8207 (2003).

[56] D. Koelling and B. Harmon, J. Phys. C: Solid State Phys **10**, 3107 (1977).

[57] S. Baroni, S. De Gironcoli, and A. Dal, Rev. Mod. Phys **73**, 515 (2001).

[58] A. Togo, F. Oba, and I. Tanaka, Phys. Rev. B **78**, 134106 (2008).

[59] Z. Sohbatzadeh, H. A. Eivari, and D. V. Fakhrabad, Phys. B: Condens. Matter **547**, 88 (2018).

[60] W. Zhou, J. Chen, Z. Yang, J. Liu, and F. Ouyang, Phys. Rev. B **99**, 075160 (2019).

[61] Y.-C. Rao, S. Yu, and X.-M. Duan, Phys. Chem. Chem. Phys. **19**, 17250 (2017).

[62] S.-D. Guo, Phys. Chem. Chem. Phys. **20**, 7236 (2018).

[63] Y. Kuang, L. Lindsay, S. Shi, and G. Zheng, Nanoscale **8**, 3760 (2016).

[64] H. Xie, T. Ouyang, É. Germaneau, G. Qin, M. Hu, and H. Bao, Phys. Rev. B **93**, 075404 (2016).

[65] S. Wang, W. Wang, and G. Zhao, Phys. Chem. Chem. Phys. **18**, 31217 (2016).

[66] C. H. Lui, Z. Ye, C. Ji, K.-C. Chiu, C.-T. Chou, T. I. Andersen, C. Means-Shively, H. Anderson, J.-M. Wu, T. Kidd, Y.-H. Lee, and R. He, Phys. Rev. B **91**, 165403 (2015).

[67] M. Idrees, H. Din, S. Khan, I. Ahmad, L.-Y. Gan, C. V. Nguyen, and B. Amin, J. Appl. Phys. **125**, 094301 (2019).

[68] G. Rehman, S. Khan, B. Amin, I. Ahmad, L.-Y. Gan, and M. Maqbool, J. Mater. Chem. C **6**, 2830 (2018).

[69] J. R. Schaibley, H. Yu, G. Clark, P. Rivera, J. S. Ross, K. L. Seyler, W. Yao, and X. Xu, Nat. Rev. Mater. **1**, 16055 (2016).

[70] K. Kośmider and J. Fernández-Rossier, Phys. Rev. B **87**, 075451 (2013).
[71] S. Guo, Y. Wang, C. Wang, Z. Tang, and J. Zhang, Phys. Rev. B **96**, 245305 (2017).
[72] T. Hu, F. Jia, G. Zhao, J. Wu, A. Stroppa, and W. Ren, Phys. Rev. B **97**, 235404 (2018).
[73] H. Din, M. Idrees, T. A. Alrebdi, C. V. Nguyen, and B. Amin, Comput. Mater. Sci. **164**, 166 (2019).
[74] H.-P. Komsa and A. V. Krasheninnikov, Phys. Rev. B **88**, 085318 (2013).
[75] G. Henkelman, A. Arnaldsson, and H. Jónsson, Comput. Mater. Sci. **36**, 354 (2006).
[76] W. Mtangi, F. Tassinari, K. Vankayala, A. Vargas Jentzsch, B. Adelizzi, A. R. Palmans, C. Fontanesi, E. Meijer, and R. Naaman, J. Am. Chem. Soc. **139**, 2794 (2017).
[77] A. H. Castro Neto and F. Guinea, Phys. Rev. Lett. **103**, 026804 (2009).
[78] M. M. Asmar and S. E. Ulloa, Phys. Rev. Lett. **112**, 136602 (2014).
[79] F. Zheng, L. Z. Tan, S. Liu, and A. M. Rappe, Nano Lett. **15**, 7794 (2015).
[80] X. Zhang and G. Lu, Carbon **108**, 215 (2016).
[81] N. Singh and U. Schwingenschlögl, EPL **104**, 37002 (2013).
[82] C. W. Myung, S. Javaid, K. S. Kim, and G. Lee, ACS Energy Lett. **3**, 1294 (2018).
[83] Y. Ji, M. Yang, H. Lin, T. Hou, L. Wang, Y. Li, and S.-T. Lee, J. Phys. Chem. C **122**, 3123 (2018).
[84] X. Ma, X. Wu, H. Wang, and Y. Wang, J. Mater. Chem. A **6**, 2295 (2018).